

Derivation of bootstrap current fraction scaling formula for 0-D system code analysis

Ryosuke Sakai, Takaaki Fujita, Atsushi Okamoto

Nagoya University, Furo-cho, Chikusa-ku, Nagoya-city, 464-8603, Japan

High Lights

- New bootstrap fraction scaling formulas were derived using the ACCOME code.
- A set of 12,150 self-consistent equilibria with positive shear was employed.
- The best one of derived formulas is applicable in a wide range of parameters.

ABSTRACT

We constructed new scaling formulas for the bootstrap current fraction f_{BS} for tokamaks with full non-inductive operation with positive shear safety factor q profiles. A fitting database was built by the ACCOME code, which contains 12,150 cases of self-consistent equilibria with the q profiles satisfying $q(\rho) \geq 1.0$ and $q_{95} \geq 3.0$ in $0 \leq \rho < 1$, where ρ is the normalized minor radius and q_{95} is q at the 95% poloidal flux surface. From the fitting database, we derived the formulas by the multiple regression analysis. The best formula contained the inverse aspect ratio ϵ , the poloidal beta, the internal inductance, $q_{95}/q(0)$, and the profile shape indices for density and temperature as input. The Root Mean Squared Error for the fitting database of this formula was 0.025. We tested the derived formulas to three kinds of datasets and compared with the K. Gi models and the ITER Physics Design Guidelines model. The first test is for the compact neutron source with the same plasma size with the fitting database, the second (including reversed shear) and the third ones (positive shear only) are for the conventional reactor size. The best formula seems to be applicable to tokamak plasmas with a wide range of parameters.

Keywords: Bootstrap current fraction, Systems code, Reactor design, Tokamak, Spherical tokamak, Scaling

1. Introduction

The system codes are used to find the optimum reactor design and its dependence on assumptions on plasma physics and engineering constraint conditions, scanning extensive parameters. Many systems codes have been developed – for example PEC [1], PROCESS [2], TPC [3], HELIOS [4], TREND [5], SPECTRE [6], and SYCOMORE [7]. System codes have also been developed for ARIES project [8] and in KAERI [9]. The system codes consist of a zero dimensional (0-D) equations on energy balance, current balance and particle balance containing plasma physics and reactor engineering modules. One of the reasons of using 0-D equations is for simplicity and shortening of computation time to extensive parameters scans. The bootstrap current fraction f_{BS} , which is the ratio of the bootstrap current I_{BS} to the total plasma current I_p , is evaluated in system code for tokamak reactors, because f_{BS} is needed to evaluate the current drive power for sustaining the total plasma current. The validity of f_{BS}

formulas is one of the most important factors of system code for evaluation of economy of tokamak reactors. The f_{BS} is evaluated by the 0-D formulas in system code while it depends strongly on the pressure and current density profiles. Therefore, constructing an accurate f_{BS} formula for system code is a challenging subject.

The bootstrap current density at a given minor radius is roughly in proportional to the pressure gradient divided by the poloidal magnetic field. As a result, the simplest formula for f_{BS} is given by $f_{BS} \propto \epsilon^{0.5} \beta_p$ [10], where ϵ is the inverse aspect ratio and β_p is the poloidal beta. In more detail, the pressure profile and the profile of the safety factor q (or the current density) should be taken into account. In our previous study [11], the economy of tokamak fusion neutron source with normal conductive coil was evaluated by a system code PEC (Physics-Engineering-Cost) [1], with the f_{BS} formulas of Wong model [12]. In this formula, f_{BS} is given by β_p , ϵ and the pressure peaking factor, but no parameters related to the q profile are included.

Many f_{BS} formulas have been developed and are

Table 1 The main plasma parameters and the scanned parameters for f_{BS} fitting database. The scan parameters are shown below of the double line. Some of the other parameters are shown in Table 2.

Parameter		Value (Range)	Points
Plasma major radius [m]	R_p	2.44	1
Elongation	κ	2.30	1
Triangularity	δ	0.50	1
Central density [10^{20}m^{-3}]	n_0	1.80	1
Effective charge	Z_{eff}	2.00	1
<hr/>			
Plasma minor radius [m]	a_p	0.48-1.48	11
Central temperature [keV]	T_0	15.0-31.0	5
Density profile index	α_n	0.35-1.10	4
Temperature profile index	α_T	0.60-2.40	4
Distance between the inner and outer beam lines [m]	$\Delta_{\text{NB}}^{\text{out}}$	$0.10a_p$ - $0.40a_p$	4
Tangent distance from R_p of the inner beam line [m]	$\Delta_{\text{NB}}^{\text{in}}$	$0.05a_p$ - $0.40a_p$	8

available in system codes – for example Nevins model [13], ITER Physics Design Guidelines (IPDG) model [14], ARIES model [8], Andrade model [15], Wilson model [16], Hoang model [17], Wong model [12], and Gi model [18]. It is also possible to evaluate f_{BS} by using the formulas for coefficients in the equations for the local bootstrap current density given in [19] in PROCESS code [20]. K. Gi et al. derived new f_{BS} formulas for the system code analysis based on 8,800 database built by the bootstrap current density calculation module in ACCOME (Analyzer for Current Drive Consistent with Magnetohydrodynamics Equilibrium) code [21] and compared them with existing f_{BS} formulas [18]. In ACCOME code, I_{BS} is evaluated for multi-species ions, including the fast ions, on the basis of the Hirshman-Sigmar moment approach of the neoclassical theory [21]. The calculation of the various currents including the bootstrap current and the externally driven current and the calculation of the magnetohydrodynamics (MHD) equilibrium are repeated until the total plasma current density profile is converged. Thus the plasma current density profile consistent with the MHD equilibrium is obtained. In K. Gi models, the q_{95}/q_0 was included as a

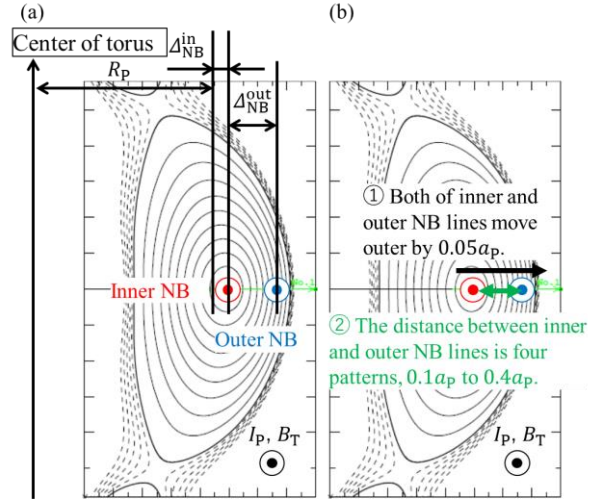


Fig. 1 Detailed description of the beam lines scan. (a) The geometric definitions of $\Delta_{\text{NB}}^{\text{out}}$ and $\Delta_{\text{NB}}^{\text{in}}$. (b) The description of the movement of the beam lines.

parameter describing the q profile. Here q_{95} is the q at the 95% poloidal flux surface while q_0 is the q at the magnetic axis. The proposed formulas are favorable to use for system code. In the validity evaluation, however, they have more than 20 % errors in several cases [18]. The errors seem to be caused since the formula was made from the results where equilibrium convergence was not considered in the ACCOME analysis in order to conduct a large number of parameter scan.

The difficulty in including parameters related to the q profile into the f_{BS} formula comes from a large variety of q profiles in tokamak plasmas. For instance, even when q_{95}/q_0 is common, the value of q around the mid radius can be significantly different between the positive shear case where q increases monotonically with the radius and the reversed shear case where q profile has a minimum, q_{min} between the axis and the surface. In [18] it is reported that the Wilson formula [16], containing current density profile index for a function of the normalized poloidal flux, most successfully predicts f_{BS} , but this formula is not suited for system code because the current density profile index for a function of the normalized poloidal flux is not usually used in system code or in the experiment database. This problem will be diminished if we exclude the reversed shear plasmas

Table 2 The main plasma parameters in each a_p , which are not shown in Table 1.

Plasma minor radius [m]	a_p	0.48	0.58	0.68	0.78	0.88	0.98	1.08	1.18	1.28	1.38	1.48
Aspect ratio	A	5.08	4.21	3.59	3.13	2.77	2.49	2.26	2.07	1.91	1.77	1.65
Inverse aspect ratio	ε	0.20	0.24	0.28	0.32	0.36	0.40	0.44	0.48	0.52	0.57	0.61
Total plasma current [MA]	I_p	4.55	5.46	6.17	6.97	7.78	8.59	9.40	9.40	9.40	9.40	9.40
Toroidal magnetic field [T]	B_T	19.0	18.1	15.3	13.4	12.5	10.6	7.75	6.49	5.52	4.75	4.13
Poloidal beta	β_p	0.39-	0.41-	0.45-	0.52-	0.54-	0.59-	0.66-	0.73-	0.82-	0.91-	1.10-
		2.45	2.44	2.52	2.61	2.65	2.60	2.41	2.36	2.82	2.53	2.65
Internal inductance	l_i	0.41-	0.39-	0.33-	0.31-	0.29-	0.28-	0.30-	0.29-	0.29-	0.31-	0.28-
		1.21	1.16	1.17	1.18	1.15	1.17	1.14	1.10	1.16	1.09	1.03

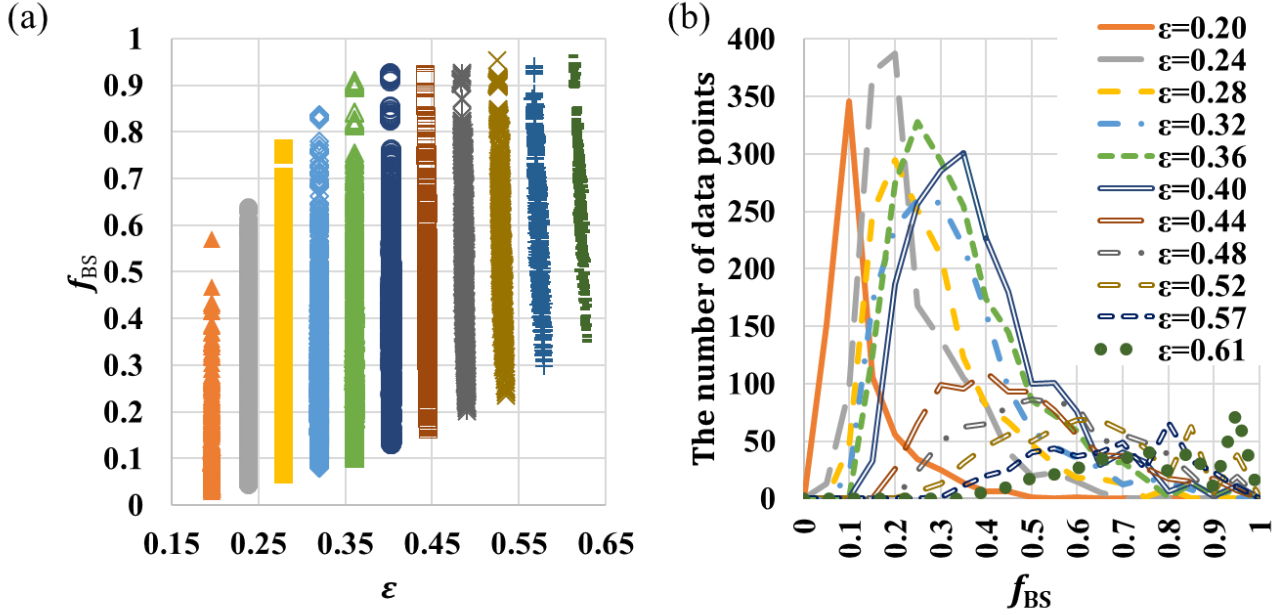


Fig. 2 (a) The dependence of f_{BS} on ϵ , and (b) the distribution function.

for the target of the formula. The reversed shear plasma has a potential of high confinement, high f_{BS} and eventually high beta but adopting it to reactors seems to be challenging because very careful control of pressure and q profiles are needed to sustain it. In order to get high confinement, a strong internal transport barrier (ITB) is needed to be located at a large minor radius. Then current profile control is needed to realize the large radius of q_{min} since strong ITBs appear inside the radius of q_{min} [22]. It was reported that the careful control of pressure and current profiles is required, in particular when q_{min} crossed integer values, for the stable sustainment of the reversed shear plasma with large f_{BS} [23]. It was also reported that the $n = 1$ kink mode, the ballooning mode and the infernal mode could be stabilized by moving the radius of q_{min} away from the steep pressure gradient region in numerical analysis [24]. In fact, the positive or weak shear plasma is often assumed in recent tokamak Demonstration Power Plant (DEMO) design studies [25]. In this study, we construct new f_{BS} formulas for system code analysis concentrating on the positive shear plasmas using the ACCOME code [21]. We use the internal inductance l_i and/or q_{95}/q_0 to include the effects of q profile on f_{BS} . The rest of the paper is organized as follows. In section 2, building a fitting database and deriving f_{BS} formulas from it are described. In section 3, validity test of the derived formulas is shown. The summary and conclusion are provided in section 4.

2. Parameter scan for the derivation of scaling formula of f_{BS}

2.1. Scan methodology

We created a fitting database for the f_{BS} using the ACCOME code [21]. In this study, equilibria with the fully non-inductively driven conditions with neutral beam (NB) injection only are calculated, where the total plasma current is sustained by NB driven current together with the bootstrap current and the diamagnetic current. Note that the toroidal component of the diamagnetic current I_{DI} was included in f_{BS} in our fitting database; $f_{BS} = (I_{BS} + I_{DI})/I_P$. In ACCOME code, I_{DI} is calculated based on formula given in [26]. The density n and temperature T profiles were fixed and given by equations shown below,

$$n(\rho) = n_0(1 - \rho^2)^{\alpha_n} \quad (1)$$

$$T(\rho) = T_0(1 - \rho^2)^{\alpha_T} \quad (2)$$

where ρ is the normalized minor radius. The electron temperature and the ion temperature were assumed to be equal and these profiles were fixed since the particle and heat transport was not solved. In this scan, we used temperature and density profiles relevant to L-mode plasmas, namely without edge pedestals, for simplicity. Using H-mode relevant profiles with edge pedestals would require additional parameters, which would lead to more complicated f_{BS} formulas. The profiles without edge pedestal are used in PEC [1] and also in several systems codes (TPC [3], SPECTOR [6]). Many of the other systems codes (e.g. PROCESS [2] and TREND [5]) also have the option of L-mode profiles. The deuterium beam was injected into the deuterium-tritium plasma. As impurity, fully-stripped carbon ions were included in the plasma with the effective ion charge Z_{eff} of 2.0, which resulted in the ratio of fuel ion (deuterons and tritons) density to the electron density of 0.80. The expected dominant impurities

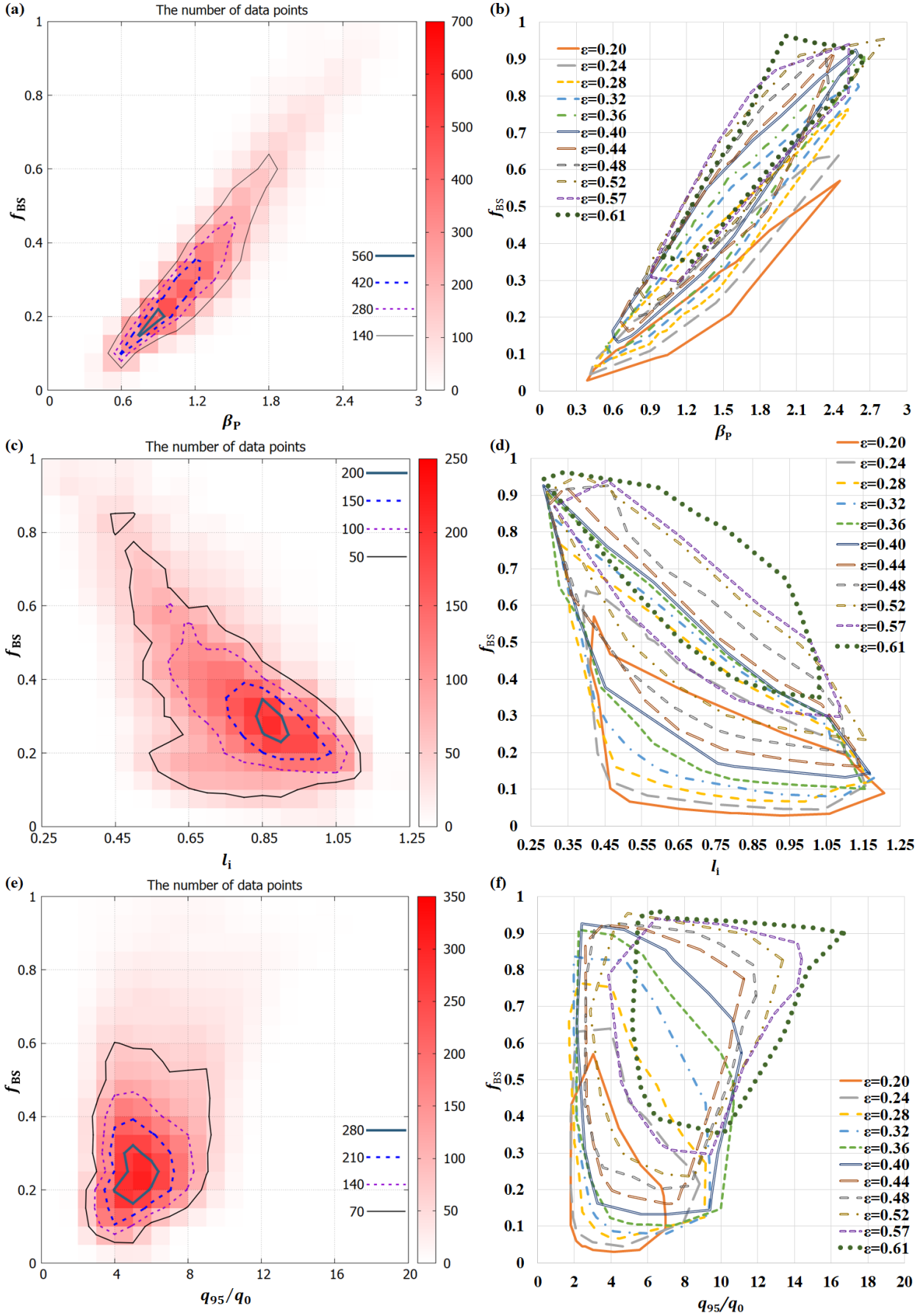


Fig. 3 The contours of the number of data points in (a) f_{BS} and β_P , (c) f_{BS} and l_i and (e) f_{BS} and q_{95}/q_0 . The boundaries of the domain of the data points of each ε in (b) f_{BS} and β_P , (d) f_{BS} and l_i , and (f) f_{BS} and q_{95}/q_0 .

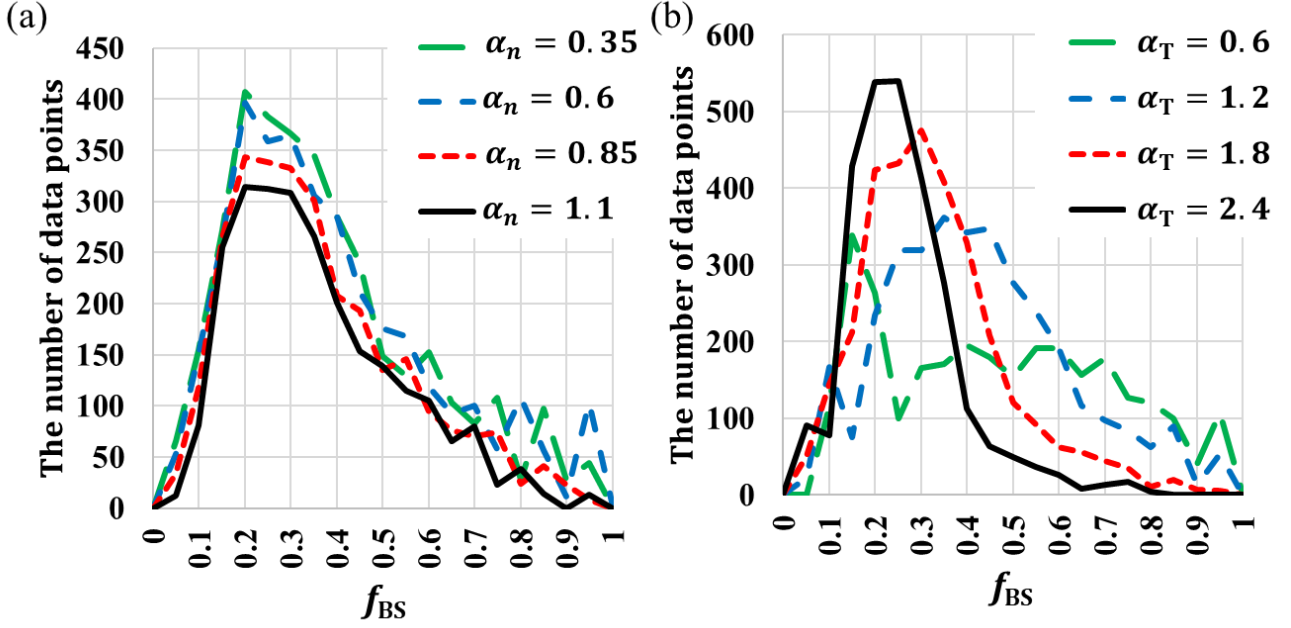


Fig. 4 The distribution function in f_{BS} for each (a) α_n and (b) α_T .

in DEMO reactors are helium and seeded impurity such as argon. We used carbon ions as those with an intermediate charge number between helium ion and argon ion.

The scanned parameters and ranges are shown in Table 1. We tried to construct a scaling of f_{BS} as a function of ε , β_p , α_n , α_T and parameters related to the q profile. We used l_i and/or q_{95}/q_0 as parameters related to the q profile. The plasma major radius R_p and the elongation κ and triangularity δ of the plasma cross-section were fixed; $R_p = 2.44$ m, $\kappa = 2.30$, $\delta = 0.50$. These values are based on the parameters used for study on tokamak neutron source in [11]. Though this R_p is smaller than ITER and expected typical future fusion reactors, it would not matter since most of the existing f_{BS} formulas [8, 14-18] do not depend on the absolute size of the plasma (R_p). In this study, we tested the derived formula for larger-size plasmas, which will be presented in section 3.2 and 3.3. The plasma minor radius a_p was changed to scan ε . The parameters for each a_p are shown in Table 2. The central temperature T_0 was changed in a range shown in Table 1 to scan β_p for each ε , while the central density n_0 was fixed to be $1.8 \times 10^{20} \text{m}^{-3}$. The plasma current I_p was reduced in a low ε range to obtain sufficiently high β_p . The toroidal field B_T was changed depending on a_p to obtain q profiles such that $q_{95} \geq 3.0$ and $q(\rho) \geq 1.0$ in $0 \leq \rho < 1$.

Two co-tangential horizontal NB units with the beam radius of 0.25 m were employed. The beam energy was 800 keV for both units. The NB power was automatically regulated for full non-inductive current drive keeping the power ratio between them 50:50. The beam lines were both on the equator plane and the tangent radii were scanned in order to change the q profile. The detailed description of the beam lines scan is shown in Fig. 1. The scan range was

determined considering the requirement of the q profiles: positive shear with $q_{95} \geq 3.0$ and $q(\rho) \geq 1.0$ in $0 \leq \rho < 1$.

2.2. Scan results and the derivation of scaling formula of f_{BS}

As the fitting database, we selected 12,150 data points satisfying the condition of the q profile, namely $q_{95} \geq 3.0$ and $q(\rho) \geq 1.0$ in $0 \leq \rho < 1$ with positive shear, from ACCOME runs with successful convergence of the equilibrium calculation and the current calculation. Distributions of parameters in the fitting database are shown in Figs. 2, 3 and 4. Fig. 2 shows ranges in f_{BS} as functions of ε and the distribution of the data points for each ε . Sufficiently large ranges in f_{BS} are obtained for each ε , though data points tend to be accumulated in the low f_{BS} region for small ε cases. Fig. 3 shows ranges in f_{BS} in the whole fitting database and also the boundaries of the rough domain of the data points for each ε , as functions of β_p , l_i and q_{95}/q_0 . As shown in Figs. 3 (a), (c), and (e), the density of the data points is high around $0.45 \leq \beta_p \leq 1.05$, $0.75 \leq l_i \leq 1.0$, $4.0 \leq q_{95}/q_0 \leq 6.0$, with $f_{BS} \leq 0.4$. The boundaries of the domains of the data points shown in Figs. 3 (b), (d), and (f) are drawn by connecting the outermost data points for each ε . Positive β_p dependence of f_{BS} with strong correlation is found in Figs. 3 (a) and (b). The f_{BS} has a negative dependence on l_i , with modest correlation, as shown in Figs. 3 (c) and (d). A sufficiently large range in f_{BS} is obtained for each value of q_{95}/q_0 with no clear dependence on q_{95}/q_0 as shown in Figs. 3 (e) and (f). The f_{BS} is larger for larger ε at fixed β_p , l_i or q_{95}/q_0 as shown in Figs. 3 (b), (d), and

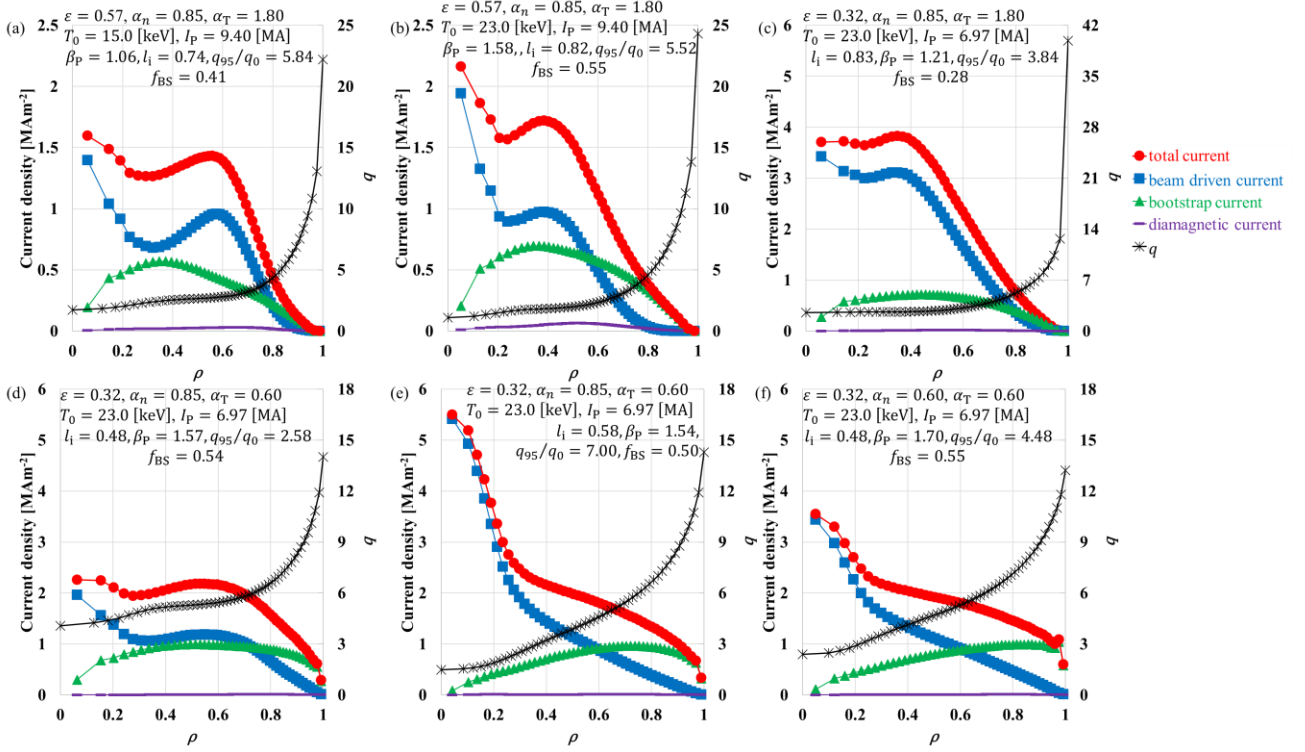


Fig. 5 (a)-(f) Examples of the radial profiles of the current density and the safety factor in the fitting database.

(f). Finally, Fig. 4 shows distributions of f_{BS} for each α_n and α_T . The distribution is shifted toward lower f_{BS} for peaked temperature profiles with larger α_T , while it changes only slightly with α_n .

Fig. 5 shows examples of the radial profiles of the current density and the safety factor. In this figure, a single input parameter is mainly changed between panels. In (b), T_0 is higher than in (a), and then f_{BS} is higher. In (c), ϵ is lower than in (b), and then f_{BS} is lower. In (d), α_T is smaller than in (c), and then f_{BS} is higher. In (e), NB driven current is more peaked than in (d), and then f_{BS} is lower. In (f), α_n is lower than in (d) and then f_{BS} is higher.

In deriving scaling formula of f_{BS} , we selected (i) l_i only, (ii) q_{95}/q_0 only and (iii) both l_i and q_{95}/q_0 as parameters related to the q profile. Details are described in 2.2.1, 2.2.2, and 2.2.3 below.

2.2.1. Scaling formula using l_i

As the first attempt, we used l_i as a parameter related to the q profile.

First, we conducted multiple regression analysis for the whole fitting database to determine regression coefficients c_0 to c_5 in the following equation.

$$f_{BS} = c_0 \epsilon^{c_1} \beta_P^{c_2} l_i^{c_3} \alpha_n^{c_4} \alpha_T^{c_5} \quad (3)$$

Then, we obtained following formula.

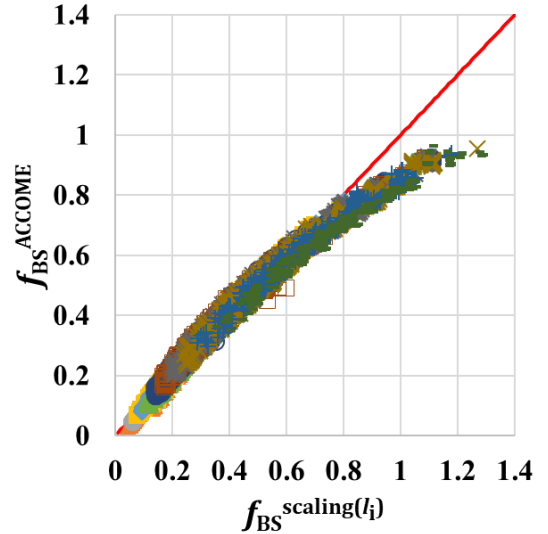


Fig. 6 The comparison between f_{BS} from the ACCOME analysis, $f_{BS}^{ACCOMME}$, and those calculated from Eq. (4), $f_{BS}^{scaling(l_i)}$. The red line is a straight line of $f_{BS}^{ACCOMME} = f_{BS}^{scaling(l_i)}$. The symbols are the same as those in Fig. 2 (a). The RMSE is 0.0403.

$$f_{BS}^{scaling(l_i)} = 0.5100 \epsilon^{0.708} \beta_P^{1.190} l_i^{-0.262} \alpha_n^{0.095} \alpha_T^{-0.1165} \quad (4)$$

The comparison between f_{BS} from the ACCOME analysis, $f_{BS}^{ACCOMME}$, and f_{BS} calculated from Eq. (4), $f_{BS}^{scaling(l_i)}$ is shown in Fig. 6. We evaluated accuracy of Eq. (4) quantitatively by the Root Mean Squared Error (RMSE)

defined by the following formula, where k is the data point number and N is the total number of the data points. As a result, RMSE is 0.0403.

$$\text{RMSE} = \sqrt{\frac{1}{N} \sum_{k=1}^N (f_{\text{BS},k}^{\text{ACCOMME}} - f_{\text{BS},k}^{\text{scaling}})^2} \quad (5)$$

As shown in Fig. 6, $f_{\text{BS}}^{\text{scaling}(l_i)}$ is systematically larger than $f_{\text{BS}}^{\text{ACCOMME}}$ and then the accuracy of the scaling becomes lower in a high f_{BS} range. To improve the accuracy, we tried to find regression coefficients c_2 to c_5 in Eq. (3) as functions of ε , not constants. We conducted multiple regression analysis in the following equation, for each ε . The results are shown by symbols in Fig. 7.

$$f_{\text{BS}} = 10^{c_0} \beta_p^{c_{\beta_p}} l_i^{c_{l_i}} \alpha_n^{c_{\alpha_n}} \alpha_T^{c_{\alpha_T}} \quad (6)$$

Next, the least-square method is used to obtain the linear approximation shown by dotted lines in Fig. 7. The results are shown below.

$$C_0 = 0.912\varepsilon - 0.968 \quad (7)$$

$$C_{\beta_p} = -1.258\varepsilon + 1.576 \quad (8)$$

$$C_{l_i} = -0.119\varepsilon - 0.370 \quad (9)$$

$$C_{\alpha_n} = 0.125\varepsilon + 0.059 \quad (10)$$

$$C_{\alpha_T} = 0.499\varepsilon - 0.255 \quad (11)$$

Substituting Eqs. (7) to (11) into Eq. (6), we obtained the following formula.

$$f_{\text{BS}}^{\text{scaling}(l_i, \varepsilon)} = 10^{0.912\varepsilon - 0.968} \beta_p^{-1.258\varepsilon + 1.576} \times l_i^{-0.119\varepsilon - 0.370} \alpha_n^{0.125\varepsilon + 0.059} \alpha_T^{0.499\varepsilon - 0.255} \quad (12)$$

The comparison between $f_{\text{BS}}^{\text{ACCOMME}}$ and f_{BS} calculated from Eq. (12), $f_{\text{BS}}^{\text{scaling}(l_i, \varepsilon)}$ is shown in Fig. 8.

The RMSE is 0.0261. The accuracy is improved in $f_{\text{BS}}^{\text{scaling}(l_i, \varepsilon)}$ compared to $f_{\text{BS}}^{\text{scaling}(l_i)}$ in particular in a high f_{BS} range.

2.2.2. Scaling formula using q_{95}/q_0

As the second attempt, we used q_{95}/q_0 , instead of l_i , for the scaling formula.

We conducted multiple regression analysis for the whole fitting database and obtained the following formula.

$$f_{\text{BS}}^{\text{scaling}(q)} = 0.858\varepsilon^{0.841} \beta_p^{1.265} (q_{95}/q_0)^{-0.183} \alpha_n^{0.068} \alpha_T^{-0.172} \quad (13)$$

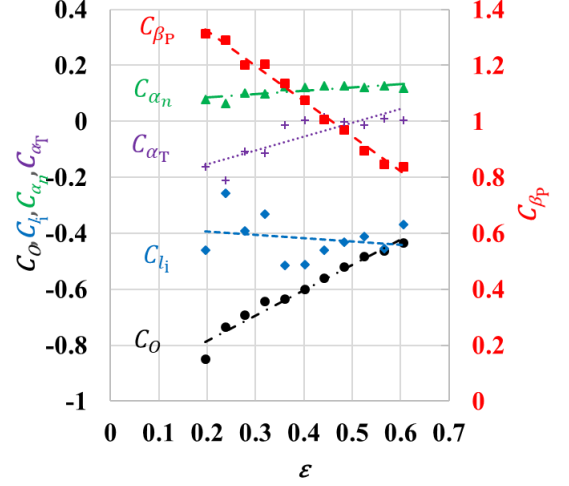


Fig. 7 The plot of the regression coefficients in Eq. (6) obtained by the multiple regression analysis in each ε . The lines show the linear approximation obtained by the least-square method.

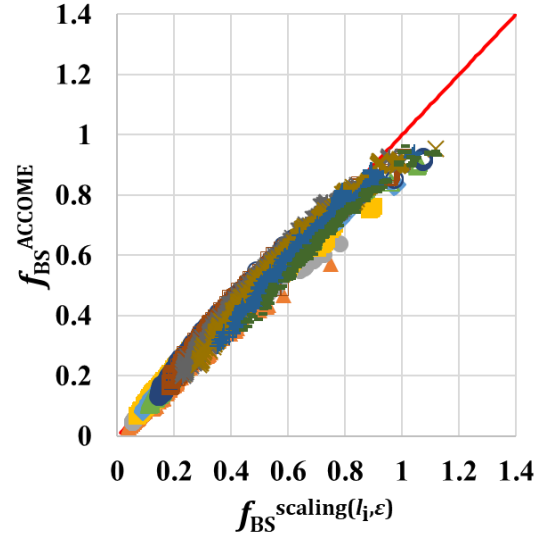


Fig. 8 The comparison between f_{BS} from the ACCOME analysis, $f_{\text{BS}}^{\text{ACCOMME}}$, and those calculated from Eq. (12), $f_{\text{BS}}^{\text{scaling}(l_i, \varepsilon)}$. The red line is a straight line of $f_{\text{BS}}^{\text{ACCOMME}} = f_{\text{BS}}^{\text{scaling}(l_i, \varepsilon)}$. The symbols are the same as those in Fig. 2 (a). The RMSE is 0.0261.

The RMSE is 0.0321, which is slightly smaller than that in $f_{\text{BS}}^{\text{scaling}(l_i)}$. Next we conducted multiple regression analysis for each ε , as we did in deriving $f_{\text{BS}}^{\text{scaling}(l_i, \varepsilon)}$. Then we obtained the following formula for f_{BS} .

$$f_{\text{BS}}^{\text{scaling}(q, \varepsilon)} = 10^{0.906\varepsilon - 0.830} \beta_p^{-0.863\varepsilon + 1.538} \times (q_{95}/q_0)^{0.133\varepsilon - 0.162} \alpha_n^{0.015\varepsilon + 0.042} \alpha_T^{0.215\varepsilon - 0.287} \quad (14)$$

The RMSE is 0.0277. The accuracy is improved in

Table 3 The comparison of RMSE for the obtained fitting database.

l_i and/or q_{95}/q_0	l_i		q_{95}/q_0		l_i and q_{95}/q_0	
Regression analysis in each ε	no	yes	no	yes	no	yes
Scaling formula	$f_{BS}^{\text{scaling}(l_i)}$	$f_{BS}^{\text{scaling}(l_i, \varepsilon)}$	$f_{BS}^{\text{scaling}(q)}$	$f_{BS}^{\text{scaling}(q, \varepsilon)}$	$f_{BS}^{\text{scaling}(l_i, q)}$	$f_{BS}^{\text{scaling}(l_i, q, \varepsilon)}$
RMSE	0.0403	0.0261	0.0321	0.0277	0.0316	0.0250

$f_{BS}^{\text{scaling}(q, \varepsilon)}$ compared to $f_{BS}^{\text{scaling}(q)}$ in particular in a high f_{BS} range, similar to the comparison between scaling $f_{BS}^{\text{scaling}(l_i, \varepsilon)}$ and $f_{BS}^{\text{scaling}(l_i)}$. The RMSE of $f_{BS}^{\text{scaling}(q, \varepsilon)}$ (0.0277) is, however, larger than that of $f_{BS}^{\text{scaling}(l_i, \varepsilon)}$ (0.0261), while the RMSE of $f_{BS}^{\text{scaling}(q)}$ (0.0321) is smaller than $f_{BS}^{\text{scaling}(l_i)}$ (0.0403).

2.2.3. Scaling formula using l_i and q_{95}/q_0

As the third attempt, we used both of l_i and q_{95}/q_0 . The formula obtained by the multiple regression analysis for the whole fitting database is shown below.

$$f_{BS}^{\text{scaling}(l_i, q)} = 0.895\varepsilon^{0.851}\beta_P^{1.274}l_i^{0.046} \times (q_{95}/q_0)^{-0.192}\alpha_n^{0.061}\alpha_T^{-0.188} \quad (15)$$

The formula obtained by multiple regression analysis for each ε is shown below.

$$f_{BS}^{\text{scaling}(l_i, q, \varepsilon)} = 10^{0.951\varepsilon - 0.948}\beta_P^{-1.226\varepsilon + 1.584}l_i^{-0.184\varepsilon - 0.282} \times (q_{95}/q_0)^{-0.042\varepsilon - 0.020}\alpha_n^{0.130\varepsilon + 0.050}\alpha_T^{0.502\varepsilon - 0.273} \quad (16)$$

Table 4 The main input and output parameters of dataset for test #1. The input parameters are shown above of the double line.

Aspect ratio	A	1.63	1.75	1.87	2.01	2.12	2.26	2.37	2.50	2.62	2.75	2.89	2.99
Inverse aspect ratio	ε	0.62	0.57	0.53	0.50	0.47	0.44	0.42	0.4	0.38	0.36	0.35	0.33
Plasma major radius [m]	R_P	1.79	1.92	2.06	2.19	2.31	2.44	2.56	2.68	2.80	2.91	3.03	3.14
Plasma minor radius [m]	a_P	1.10	1.10	1.10	1.09	1.09	1.08	1.08	1.07	1.07	1.06	1.05	1.05
Elongation	κ	2.77	2.65	2.55	2.46	2.37	2.30	2.24	2.18	2.13	2.08	2.04	2.00
Triangularity	δ	0.50	0.50	0.50	0.50	0.50	0.50	0.50	0.50	0.50	0.50	0.50	0.50
Toroidal magnetic field [T]	B_T	2.04	2.25	2.46	2.67	2.88	3.10	3.32	3.54	3.76	3.98	4.20	4.43
Total plasma current [MA]	I_P	12.00	11.33	10.75	10.24	9.80	9.40	9.04	8.72	8.43	8.17	7.92	7.70
Central density [10^{20}m^{-3}]	n_0	1.86	1.84	1.82	1.86	1.81	1.80	1.80	1.80	1.81	1.81	1.81	1.82
Central temperature [keV]	T_0	15.0	15.0	15.0	15.0	15.0	15.0	15.0	15.0	15.0	15.0	15.0	15.0
Poloidal beta	β_P	1.07	1.06	1.11	1.15	1.14	1.15	1.17	1.18	1.22	1.23	1.24	1.28
Internal inductance	l_i	0.40	0.40	0.39	0.39	0.40	0.41	0.41	0.42	0.42	0.42	0.43	0.44
Safety factor q at axis	q_0	1.06	1.18	1.24	1.16	1.13	1.09	1.17	1.28	1.24	1.34	1.43	1.59
q at the 95% poloidal flux surface	q_{95}	4.94	4.62	4.51	4.35	4.19	3.97	3.92	3.77	3.72	3.60	3.49	3.48
Ratio of q_{95} to q_0	$\frac{q_{95}}{q_0}$	4.65	3.93	3.65	3.76	3.70	3.63	3.36	2.95	3.00	2.69	2.45	2.20
Beam driven current [MA]	I_{CD}	6.68	6.40	6.00	5.60	5.45	5.29	5.01	4.85	4.65	4.56	4.44	4.29
Bootstrap current [MA]	I_{BS}	3.99	3.97	4.00	4.06	3.90	3.73	3.71	3.60	3.57	3.43	3.31	3.26
Diamagnetic current [MA]	I_{DI}	1.33	1.01	0.79	0.67	0.55	0.46	0.39	0.34	0.29	0.26	0.22	0.20
Bootstrap current fraction	f_{BS}	0.44	0.44	0.45	0.46	0.45	0.45	0.45	0.45	0.46	0.45	0.45	0.45

The RMSE of $f_{BS}^{\text{scaling}(l_i, q)}$ is 0.0316, which is smaller than that of $f_{BS}^{\text{scaling}(l_i)}$ and is slightly smaller than that of $f_{BS}^{\text{scaling}(q)}$. The RMSE of $f_{BS}^{\text{scaling}(l_i, q, \varepsilon)}$ is 0.0250. The accuracy is improved in $f_{BS}^{\text{scaling}(l_i, q, \varepsilon)}$ compared to $f_{BS}^{\text{scaling}(l_i, q)}$ in particular in a high f_{BS} range, similar to the comparison between $f_{BS}^{\text{scaling}(l_i, \varepsilon)}$ and $f_{BS}^{\text{scaling}(l_i)}$ or between $f_{BS}^{\text{scaling}(q, \varepsilon)}$ and $f_{BS}^{\text{scaling}(q)}$.

The summary of RMSEs of six formulas derived in this study is shown in Table 3. Consequently, the scaling formula $f_{BS}^{\text{scaling}(l_i, q, \varepsilon)}$, which uses both of l_i and q_{95}/q_0 for input parameters and regression coefficients of linear functions of ε , is the most accurate, though difference in RMSE is not significant compared to $f_{BS}^{\text{scaling}(l_i, \varepsilon)}$ and $f_{BS}^{\text{scaling}(q, \varepsilon)}$. Among the formulas with constant regression coefficients, the $f_{BS}^{\text{scaling}(l_i, q)}$ using both of l_i and q_{95}/q_0 is also the most accurate, but the RMSE of $f_{BS}^{\text{scaling}(q)}$ is quite close to that of $f_{BS}^{\text{scaling}(l_i, q)}$.

3. Validity test

In this section, we present results of testing the obtained formulas for other three types of plasmas than those included in the fitting database used in the previous

Table 5 The comparison of RMSE in validity tests.

	$f_{BS}^{\text{scaling}(l_i)}$	$f_{BS}^{\text{scaling}(l_i, \epsilon)}$	$f_{BS}^{\text{scaling}(q)}$	$f_{BS}^{\text{scaling}(q, \epsilon)}$	$f_{BS}^{\text{scaling}(l_i, q)}$	$f_{BS}^{\text{scaling}(l_i, q, \epsilon)}$	$f_{BS}^{\text{K.Gi}(1)}$	$f_{BS}^{\text{K.Gi}(2)}$	$f_{BS}^{\text{K.Gi}(1)*}$	f_{BS}^{IPDG}	$f_{BS}^{\text{IPDG}*}$
test #1	0.0769	0.0693	0.0708	0.0853	0.0732	0.0685	0.0295	0.0568		0.0905	
test #2	0.1946	0.1841	0.1700	0.1910	0.1716	0.1791	0.1886	0.2186	0.1652	0.1306	0.0471
test #3	0.0761	0.0783	0.0817	0.0965	0.0846	0.0756	0.3167	0.4483		0.2779	

section, in order to see the validity of the formulas.

3.1. Validity test with the dataset of the compact neutron source (test #1)

First, we compared f_{BS} in a series of the plasma aspect ratio A scan done in the study on a tokamak neutron source in [11] (test #1). In that study, A was scanned between 1.6 and 3.0, keeping the fusion power constant. The plasma elongation κ and the normalized plasma beta β_N were given as functions of A . The plasma major radius R_P was changed so that the area of the outer blanket was constant. The density and temperature profiles were given by Eqs. (1) and (2) with $\alpha_n = 0.25$ and $\alpha_T = 1.0$. The central temperature was kept constant (15.0 keV) while the central density was changed to have a given value of β_N . We performed ACCOME analysis for 12 values of A . The deuterium beam was injected into the deuterium-tritium plasma. As impurity, fully-stripped carbon ions are included in the plasma with Z_{eff} of 2.0. We also used two co-tangential NB units, for current drive, with beam energy of 800 keV and the beam radius of 0.25 m, though the beam line of the off-axis unit was elevated from the equator plane to minimize the power required for full non-inductive current drive. We also assumed one quasi-perpendicular NB unit, for heating, with beam energy of 200 keV and the beam radius of 0.25 m. The power of heating NB was adjusted to the summation of three (two co-tangential and one quasi-perpendicular) NBs power becomes equal to the total NB power of [11] in each A .

The main input and output parameters are shown in Table 4. Note that because the quasi-perpendicular NB was added after the optimization of two co-tangential NBs, In most cases, the total plasma current was slightly smaller than the sum of its components : $I_P \leq I_{CD} + I_{BS} + I_{DI}$. The comparison of f_{BS} by ACCOME analysis, the C. P. C. Wong model [12] used in [11], f_{BS} obtained by the scaling formulas derived in this study, the K. Gi models [18], and the IPDG model [14] are shown in Fig. 9. Here, the formula of the C. P. C. Wong model, the K. Gi models, and the IPDG model are given by the equations below

$$f_{BS}^{\text{Wong}} = C_{BS}^{\text{Wong}} f_{\text{peak}}^{0.25} \beta_P \sqrt{\epsilon} \quad (17)$$

$$C_{BS}^{\text{Wong}} = 0.773 + 0.019\kappa \quad (18)$$

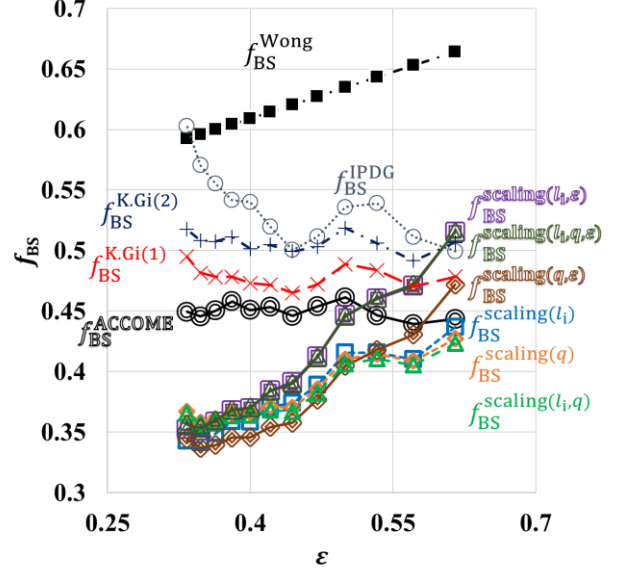


Fig. 9 The comparison of f_{BS} by ACCOME analysis, f_{BS} obtained by the scaling formulas derived in the previous section, the Wong model [12], the K. Gi models [18], and the IPDG model [14], in each ϵ of Table 4. The f_{BS}^{ACCOMe} is denoted by double-line black circles. The $f_{BS}^{\text{scaling}(l_i, \epsilon)}$, $f_{BS}^{\text{scaling}(q, \epsilon)}$, $f_{BS}^{\text{scaling}(l_i, q, \epsilon)}$ are denoted by double-line purple squares, by double-line dark orange diamonds, and by double-line dark green triangles, respectively. The $f_{BS}^{\text{scaling}(l_i)}$, $f_{BS}^{\text{scaling}(q)}$, $f_{BS}^{\text{scaling}(l_i, q)}$ are denoted by the same symbols but with a single line and light colours, respectively. The $f_{BS}^{\text{K.Gi}(1)}$, $f_{BS}^{\text{K.Gi}(2)}$, f_{BS}^{IPDG} and f_{BS}^{Wong} are denoted by red crosses, purple pluses, purple circles, and solid black squares, respectively.

$$f_{\text{peak}} = \left(\int_0^1 (1 - \rho^2)^{\alpha_T} (1 - \rho^2)^{\alpha_n} d\rho \right)^{-1} \quad (19)$$

$$f_{BS}^{\text{K.Gi}(1)} = C_{BS}^{\text{K.Gi}(1)} \epsilon^{0.4} \beta_P \quad (20)$$

$$C_{BS}^{\text{K.Gi}(1)} = 0.474 \alpha_P^{0.974} \alpha_T^{-0.416} Z_{\text{eff}}^{0.178} (q_{95}/q_0)^{-0.133} \quad (21)$$

$$f_{BS}^{\text{K.Gi}(2)} = C_{BS}^{\text{K.Gi}(2)} \epsilon^{0.258} \beta_P \quad (22)$$

$$C_{BS}^{\text{K.Gi}(2)} = 0.382 \alpha_P^{0.974} \alpha_T^{-0.416} Z_{\text{eff}}^{0.178} \quad (23)$$

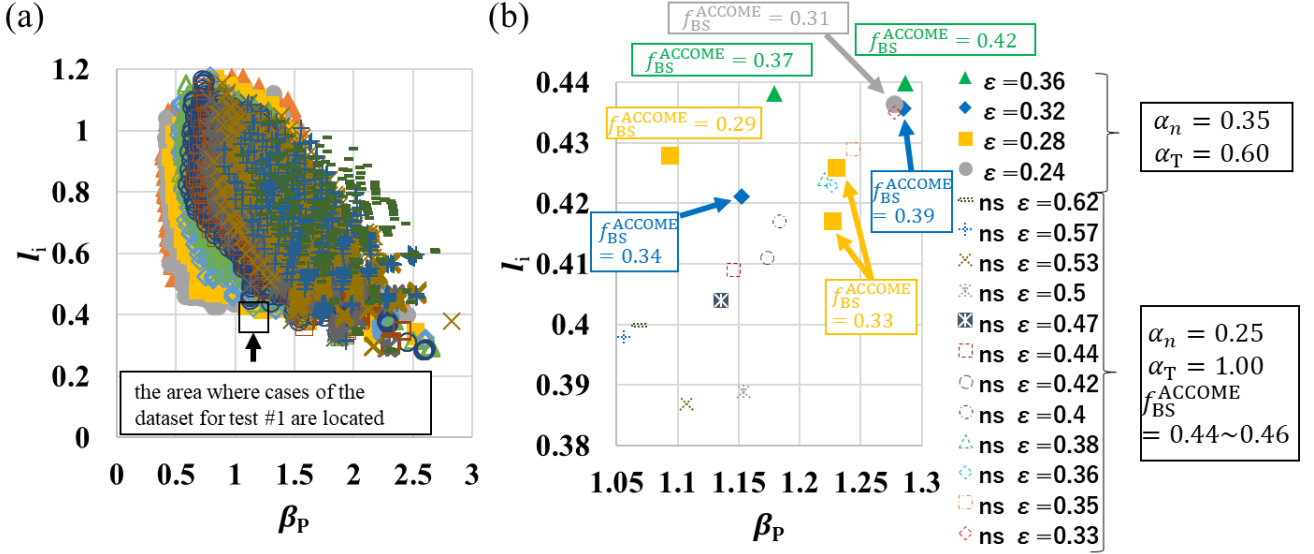


Fig. 10 (a) Distribution of β_p and l_i in the fitting database. The symbols are the same as those in Fig. 2 (a). (b) Distribution of β_p and l_i inside the square shown in (a). The closed symbols denote the data points in the fitting database, while the open symbols denote the cases in the dataset for test #1.

$$f_{BS}^{IPDG} = C_{BS}^{IPDG} (\varepsilon^{0.5} \beta_p)^{1.3} \quad (24)$$

$$C_{BS}^{IPDG} = 1.32 - 0.235(q_{95}/q_0) + 0.0185(q_{95}/q_0)^2 \quad (25)$$

where $\alpha_p = \alpha_n + \alpha_T$.

The comparison of RMSE in test #1 is shown in the first row of Table 5. The RMSEs by our formulas are in 0.069 to 0.085, the smallest one of which is by $f_{BS}^{scaling(l_i, q, \varepsilon)}$. The K. Gi model (1) [18] has the lowest RMSE for test #1. As shown in Fig. 9, our formulas have a positive dependence on ε in contrast to nearly flat values by the ACCOME analysis.

Fig. 10 (a) shows distribution of β_p and l_i in the fitting database. The cases of the dataset for test #1 are located inside the square shown in the figure. These cases are located at the boundary of the region covered by the fitting database. The enlarged view inside this area ($1.05 \leq \beta_p \leq 1.3$ and $0.38 \leq l_i \leq 0.44$) is shown in Fig. 10 (b). More than half of the cases in the dataset for test #1 are out of the region of the fitting database. In this area, furthermore, the fitting database contains data points with $0.24 \leq \varepsilon \leq 0.36$, $\alpha_n = 0.35$ and $\alpha_T = 0.60$ only while the cases of the dataset for test #1 have $0.33 \leq \varepsilon \leq 0.62$, $\alpha_n = 0.25$ and $\alpha_T = 1$. This mismatching in the input parameters (β_p , l_i , ε , α_n and α_T) would be a cause of relatively larger errors of our formulas than that of K. Gi models in test #1.

The Wong model used in [11] gives substantially larger f_{BS} than the ACCOME analysis. The device parameters obtained in [11] may be affected if we use the correct f_{BS} . We analyzed the typical case in [11] by using the ACCOME code. The results are shown in Appendix A.

3.2. Validity test with the dataset used to check the

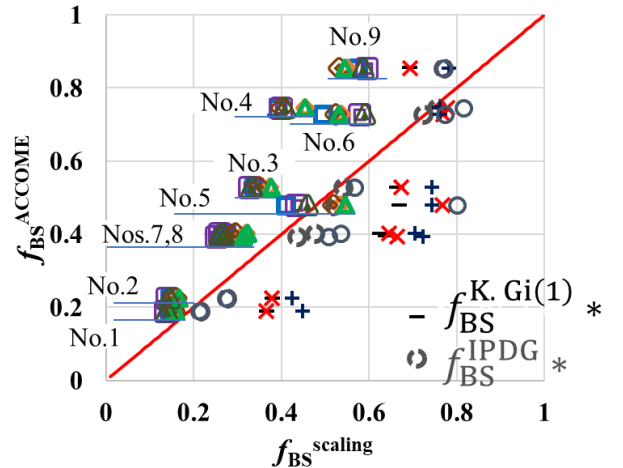


Fig. 11 The comparison between $f_{BS}^{ACCOMME}$ and $f_{BS}^{scaling}$ (our scaling formulas, $f_{BS}^{K.Gi(1)}$, $f_{BS}^{K.Gi(2)}$, $f_{BS}^{K.Gi(1)*}$, f_{BS}^{IPDG} , and f_{BS}^{IPDG*}) for nine cases (No. 1 to No. 9) in the dataset used in [18] for test #2. The symbols without the legends in this figure are the same as those in Fig. 9.

validity of the K. Gi model (test #2)

Next, we tested our scaling formulas for the dataset used in [18] (test #2), which consists of nine cases (equilibrium No. 1 to No. 9). The parameters of each case are shown in Table 4 in [18]. This dataset has the relatively larger device size (R_p) than that of the fitting database, with wide ranges of the input parameters of our formulas (ε , β_p , l_i , q_{95}/q_0 , α_n , and α_T). It also has the case of reversed shear. The main plasma parameters of Nos. 3, 4, 7 and 9, as

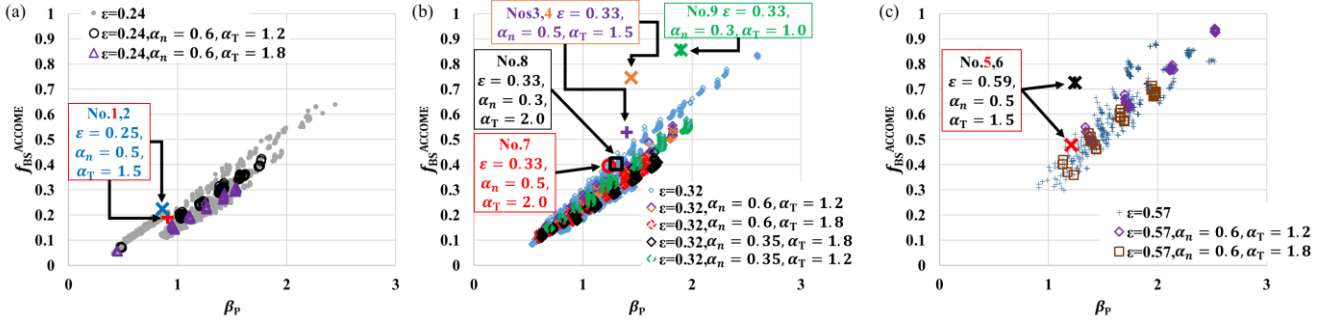


Fig. 12 The dependence of $f_{BS}^{ACCOMME}$ on β_p of the fitting database, (a) for $\varepsilon = 0.24$, with the cases of Nos. 1 and 2 ($\varepsilon = 0.25$) for test #2, (b) for $\varepsilon = 0.32$, with the cases of Nos. 3, 4, 7, 8 and 9 ($\varepsilon = 0.33$) for test #2, (c) for $\varepsilon = 0.57$, with the cases of Nos. 5 and 6 ($\varepsilon = 0.59$) for test #2.

the exemplification of test #2, are shown in Table 6. The results are shown in Fig. 11. As the values of $f_{BS}^{ACCOMME}$, $f_{BS}^{K.Gi(1)}$, $f_{BS}^{K.Gi(2)}$, $f_{BS}^{K.Gi(1)*}$, f_{BS}^{IPDG} , and f_{BS}^{IPDG*} , those shown in Table 5 in [18] are used. Here, $f_{BS}^{K.Gi(1)*}$ and f_{BS}^{IPDG*} are f_{BS} obtained by the formula based on $f_{BS}^{K.Gi(1)}$ and f_{BS}^{IPDG} , respectively, where q_{95}/q_0 is replaced with q_{95}/q_{min} to consider reversed shear [18]. The $f_{BS}^{K.Gi(1)*}$ and f_{BS}^{IPDG*} are exactly equal to $f_{BS}^{K.Gi(1)}$ and f_{BS}^{IPDG} , respectively, for positive shear cases (Nos. 1, 2 and 9). In evaluating f_{BS} by our formulas including q_{95}/q_0 , namely $f_{BS}^{scaling(q)}$, $f_{BS}^{scaling(q,\varepsilon)}$, $f_{BS}^{scaling(l_i,q)}$, and $f_{BS}^{scaling(l_i,q,\varepsilon)}$, not q_{95}/q_{min} but q_{95}/q_0 was used. Since our scaling formulas have negative dependence on q_{95}/q_0 , and $q_{95}/q_{min} > q_{95}/q_0$, the values by our scaling formulas will become smaller and then lose the accuracy if q_{95}/q_{min} is used in place of q_{95}/q_0 . As shown in Fig. 11, most of our scaling formulas underestimate f_{BS} in this dataset. The largest discrepancy is found for No. 4. For this case, our scaling formulas predict about 40% of f_{BS} while the f_{BS} by ACCOME was about 75%. The comparison of RMSE in test #2 is shown in the second row of Table 5. The RMSEs by our formulas are in 0.170 to 0.195, the smallest one of which is by $f_{BS}^{scaling(q)}$. The smallest RMSE in tested formulas is 0.047 by f_{BS}^{IPDG*} .

The dependence of $f_{BS}^{ACCOMME}$ on β_p of the fitting database, is shown in Fig. 12 for each ε , together with that of the dataset for test #2. The plots of Nos. 1, 2, 5, 7 and 8 are included or are close to the region of the fitting database. In contrast, as shown in Figs. 12 (b) and (c), the plots of Nos 3, 4, 6 and 9 are apart from the region of the fitting database. This seems to cause the relatively large errors of our scaling for these cases, compared to the other cases, as shown in Fig. 11. The profiles of the data points in the fitting database, which have parameters close to those of Nos. 3, 4, 7, and 9, are shown in Figs. 13 (a), (b), (c), and (d), respectively (see also Table 6). The values of f_{BS} of these data points, shown in corresponding panels of Fig. 13, are close to $f_{BS}^{scaling}$ of our scaling formulas shown by the horizontal axis in Fig. 11. The q profile of No. 4 is reversed shear one, generated by the NB driven current density profile

with a single beam line, whose peak is around $\rho = 0.8$ (as shown in Fig. 3 (d) in [18]). In contrast, the q profile shown in Fig. 13 (b) is positive shear one since our fitting database consists of positive shear equilibria only. The No. 6 is also reversed shear (as shown in Fig. 3 (f) in [18]). This difference in the q profile seems to be a cause of large discrepancy for Nos. 4 and 6. As for Nos. 3 and 9, profiles of the NB driven current are different. It is broader in Figs. 13 (a) and (d) than in Nos. 3 and 9 (as shown in Figs. 3 (c) and (i) in [18]), respectively. This is because a single beam line is used in Nos. 3 and 9, while two beam lines are used in all data points of our fitting database. This seems to cause different f_{BS} with close ε, β_p , and l_i (the shape of the total current profile), in weak shear or positive shear plasmas. On the other hand, the peak of the NB driven current profiles of Nos. 5, 7, and 8 are located around $\rho = 0.3$ and therefore the profiles of Nos. 5, 7, and 8 are broader than those of Nos. 3 and 9 (as shown in Figs. 3 (c), (e), (g), (h), and (i) in [18]). It is expected that we have data points with close NB driven current profiles in the fitting database for such cases. An example is shown in Fig. 13 (c), where the NB driven current profile, as well as $\varepsilon, \beta_p, l_i$, and α_n , are similar to those of No. 7. In Nos. 1 and 2, where the inductive current is included [18], the externally driven current (the summation of the beam driven current and the inductive current) is also broad. The broad externally driven current in Nos. 1, 2, 5, 7, and 8 seems to be a cause of good agreement of our scaling formulas for these cases.

Consequently, the difference of the profile of the safety factor and the beam driven current (or summation of the externally driven currents) seems to be a cause of large discrepancy for Nos. 3, 4, 6, and 9 in test #2. It should be noted, however, our formulas have similar RMSE (0.1700-0.1946) as that of the K. Gi formulas (0.1652 and 0.2186) even in test #2.

3.3. Validity test with the dataset with only positive shear (test #3)

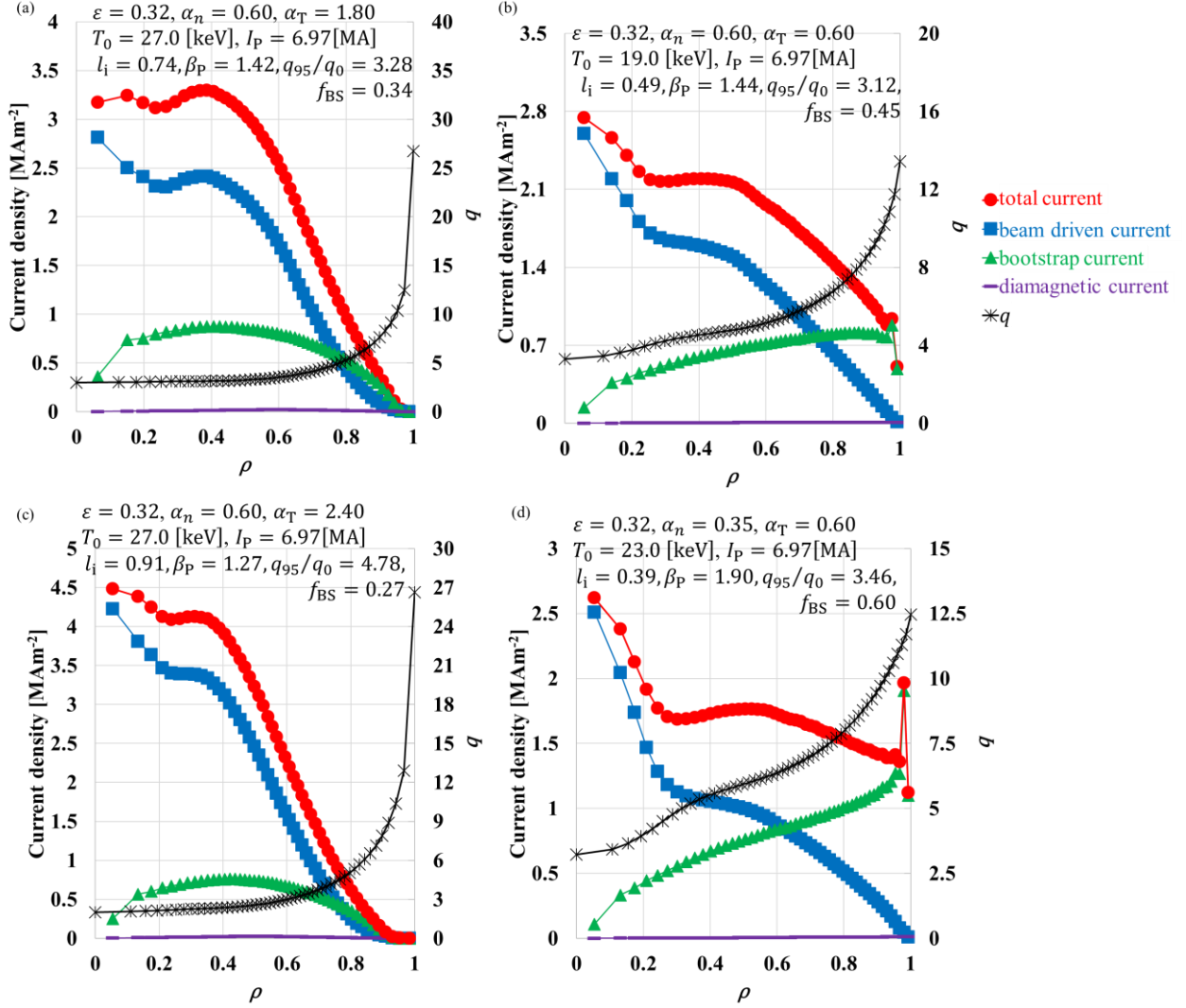


Fig. 13 The profiles of the data points from the fitting database, where parameters are close to, (a) No.3 (in $\varepsilon, \beta_P, l_i, \alpha_n, \alpha_T$, and q_{95}/q_0), (b) No.4 (in $\varepsilon, \beta_P, l_i$, and α_n), (c) No.7 (in $\varepsilon, \beta_P, l_i$, and α_n), and (d) No.9 (in $\varepsilon, \beta_P, l_i$, and α_n).

The dataset used in the test #2 contains reversed shear cases as shown in Fig. 3 in [18], while our scaling formulas are derived from our fitting database without reversed shear cases. To test the formulas for positive shear plasmas, another dataset was made based on dataset used in [18] (test #3) by the ACCOME analysis, where conditions on NB injection were adjusted to have positive shear ($q(\rho) \geq 1.0$ and $q_{95} \geq 3.0$ in $0 \leq \rho < 1$). The main plasma parameters are shown in Table 7. All of types in this study satisfied full non-inductive current drive conditions, while Nos. 1 and 2 of [18] included inductive current. We used the same values as those in the dataset in [18] for $R_P, a_P, \kappa, \delta, I_P$, the central density, α_n, α_T , and Z_{eff} . The B_T was increased from that of [18] except in (III), (IV), and (IX), to achieve $q_{95} \geq 3.0$ and $q(\rho) \geq 1.0$ in $0 \leq \rho < 1$. The two deuterium beam was scanned as we did for the fitting database (shown in section 2.1, Fig. 1, and Table 1) in each

Table 6 The main plasma parameters of Nos. 3, 4, 7 and 9 for test #2, referred to [18]. The q_{95}/q_0 is derived from $f_{\text{BS}}^{\text{K.Gi}(1)}$ and the other input values are shown in Tables 4 and 5 in [18].

	No.3	No.4	No.7	No.9	
Plasma major radius [m]	R_P	5.00	5.00	5.00	5.00
Plasma minor radius [m]	a_P	1.67	1.67	1.67	1.67
Inverse aspect ratio	ε	0.33	0.33	0.33	0.33
Central temperature [keV]	T_0	20.0	20.0	20.0	20.0
Density profile index	α_n	0.50	0.50	0.50	0.30
Temperature profile index	α_T	1.50	1.50	2.00	1.00
Total plasma current [MA]	I_P	7.00	7.00	7.00	7.00
Poloidal beta	β_P	1.40	1.44	1.24	1.90
Internal inductance	l_i	0.74	0.49	0.93	0.39
Ratio of q_{95} to q_0	$\frac{q_{95}}{q_0}$	3.29	1.37	3.05	3.98

Table 7 The main plasma parameters of dataset for test #3. The output parameters are shown in below of the double line.

		(I)	(II)	(III)	(IV)	(V)	(VI)	(VII)	(VIII)	(IX)
Plasma major radius [m]	R_P	5.00	5.00	5.00	5.00	5.00	5.00	5.00	5.00	5.00
Plasma minor radius [m]	a_P	1.25	1.25	1.67	1.67	2.94	2.94	1.67	1.67	1.67
Aspect ratio	A	4.00	4.00	2.99	2.99	1.70	1.70	2.99	2.99	2.99
Inverse aspect ratio	ε	0.25	0.25	0.33	0.33	0.59	0.59	0.33	0.33	0.33
Elongation	κ	1.36	1.39	1.84	1.92	1.77	1.94	1.75	1.76	2.07
Triangularity	δ	0.33	0.35	0.28	0.39	0.28	0.43	0.19	0.20	0.50
Central density [10^{20}m^{-3}]	n_0	0.80	0.80	1.00	1.00	1.50	1.50	1.00	1.00	1.00
Central temperature [keV]	T_0	20.0	20.0	20.0	30.0	30.0	35.0	20.0	20.0	20.0
Troidal magnetic field [T]	B_T	7.50	7.50	5.30	4.00	4.26	3.29	6.00	6.00	4.00
Density profile index	α_n	0.50	0.50	0.50	0.50	0.50	0.50	0.50	0.30	0.30
Temperature profile index	α_T	1.50	1.50	1.50	1.50	1.50	1.50	2.00	2.00	1.00
Effective charge	Z_{eff}	1.80	1.80	1.80	1.80	1.80	1.80	1.80	1.80	1.80
Total plasma current [MA]	I_P	5.50	5.50	7.00	7.00	20.0	20.0	7.00	7.00	7.00
Poloidal beta	β_P	1.09-	1.12-	1.74-	2.88-	1.57-	2.13	1.45-	1.52-	2.71-
		1.11	1.13	1.75	2.90	1.58		1.47	1.55	2.74
Internal inductance	l_i	0.85-	0.85-	0.66-	0.56-	0.81-	0.71-	0.80-	0.77-	0.39
		0.92	0.91	0.75	0.57	0.87	0.72	0.94	0.90	
Safety factor q at axis	q_0	1.04-	1.06-	1.04-	1.10-	1.02-	1.01-	1.22-	1.19-	1.20-
		1.21	1.26	1.86	1.76	1.27	1.05	1.63	1.58	2.89
q at the 95% poloidal flux	q_{95}	3.45-	3.60-	5.87-	5.62-	7.27-	7.82-	5.90-	5.98-	6.92
		3.46	3.61	5.92	5.63	7.40	7.84	5.91	5.99	
Ratio of q_{95} to q_0	$\frac{q_{95}}{q_0}$	2.85-	2.86-	3.19-	3.19-	5.83-	7.45-	3.62-	3.79-	2.39-
		3.31	3.39	5.65	5.12	7.15	7.71	4.85	5.03	5.75
Bootstrap current [MA]	I_{BS}	1.26-	1.29-	3.72-	5.94-	9.18-	11.9-	2.78-	2.87-	6.12-
		1.32	1.35	4.14	6.09	9.59	12.0	3.21	3.27	6.30
Diamagnetic current [MA]	I_{DI}	0.04-	0.04	0.09-	0.26-	1.12-	2.23-	0.08-	0.08-	0.15-
		0.05		0.11	0.27	1.19	2.24	0.09	0.09	0.16
Bootstrap current fraction	f_{BS}	0.24-	0.24-	0.55-	0.89-	0.52-	0.71	0.41-	0.42-	0.90-
		0.25	0.25	0.60	0.91	0.54		0.47	0.48	0.92

type. We did not fix the output parameters shown below the double line in Table 7 to the values in [18]. Types (I) and (II) correspond to conventional tokamak ($A = 3 - 4$ with relatively low beta value), types (III) and (IV) correspond to advanced tokamak ($A = 3 - 4$ with relatively high beta value), and types (V) and (VI) correspond to spherical tokamak ($A \leq 2$). In types (VII) to (IX) mainly α_n and α_T are changed from type (III). Type (II) has a broader current density profile than type (I) by changing the NB driven current profile as so in [18]. The central temperature was changed between (III) and (IV) and between (V) and (VI) to make a difference in f_{BS} , instead of including reversed shear. The typical current density and q profiles of each type of data are shown in Fig. 14. Panels (a)-(i) in Fig. 14 correspond to the types (I)-(IX) in Table 7.

The comparison between f_{BS}^{ACCOMME} and f_{BS}^{scaling} (our scaling formulas, $f_{BS}^{\text{K.Gi(1)}}$, $f_{BS}^{\text{K.Gi(2)}}$, and f_{BS}^{IPDG}) is shown in Fig. 15. The points for $f_{BS}^{\text{K.Gi(1)*}}$ and $f_{BS}^{\text{IPDG*}}$ are not included here since no reversed shear cases are included in this dataset. Note that more than one data

points are plotted for each type in the dataset because we had different equilibria by changing beam lines in each type. The K. Gi models and the IPDG model seem to overestimate f_{BS} in this dataset. The comparison of RMSE in test #3 is shown in the third row of Table 5. The RMSEs by our formulas are in 0.076 to 0.097, the smallest one of which is by $f_{BS}^{\text{scaling}(l_i, q, \varepsilon)}$. The formulas with constant regression coefficients, $f_{BS}^{\text{scaling}(l_i)}$, $f_{BS}^{\text{scaling}(q)}$, $f_{BS}^{\text{scaling}(l_i, q)}$ have values similar to those by the formulas with regression coefficients of linear function of ε , $f_{BS}^{\text{scaling}(l_i, \varepsilon)}$, $f_{BS}^{\text{scaling}(q, \varepsilon)}$, $f_{BS}^{\text{scaling}(l_i, q, \varepsilon)}$ except for (VI).

The dependence of f_{BS}^{ACCOMME} on β_P of the fitting database is shown in Fig. 16, with the cases for test #3. Except (IV) and (IX), the plots for test #3 are in the region of the fitting database. As shown in Fig. 16 (b), while the plots of (IV) and (IX) are slightly out of the region of the fitting database, these are located on a line extended from the fitting database region and then it seems to be easy to predict f_{BS} of these two cases from the fitting database. In the cases for test #3, two beam lines were used and only

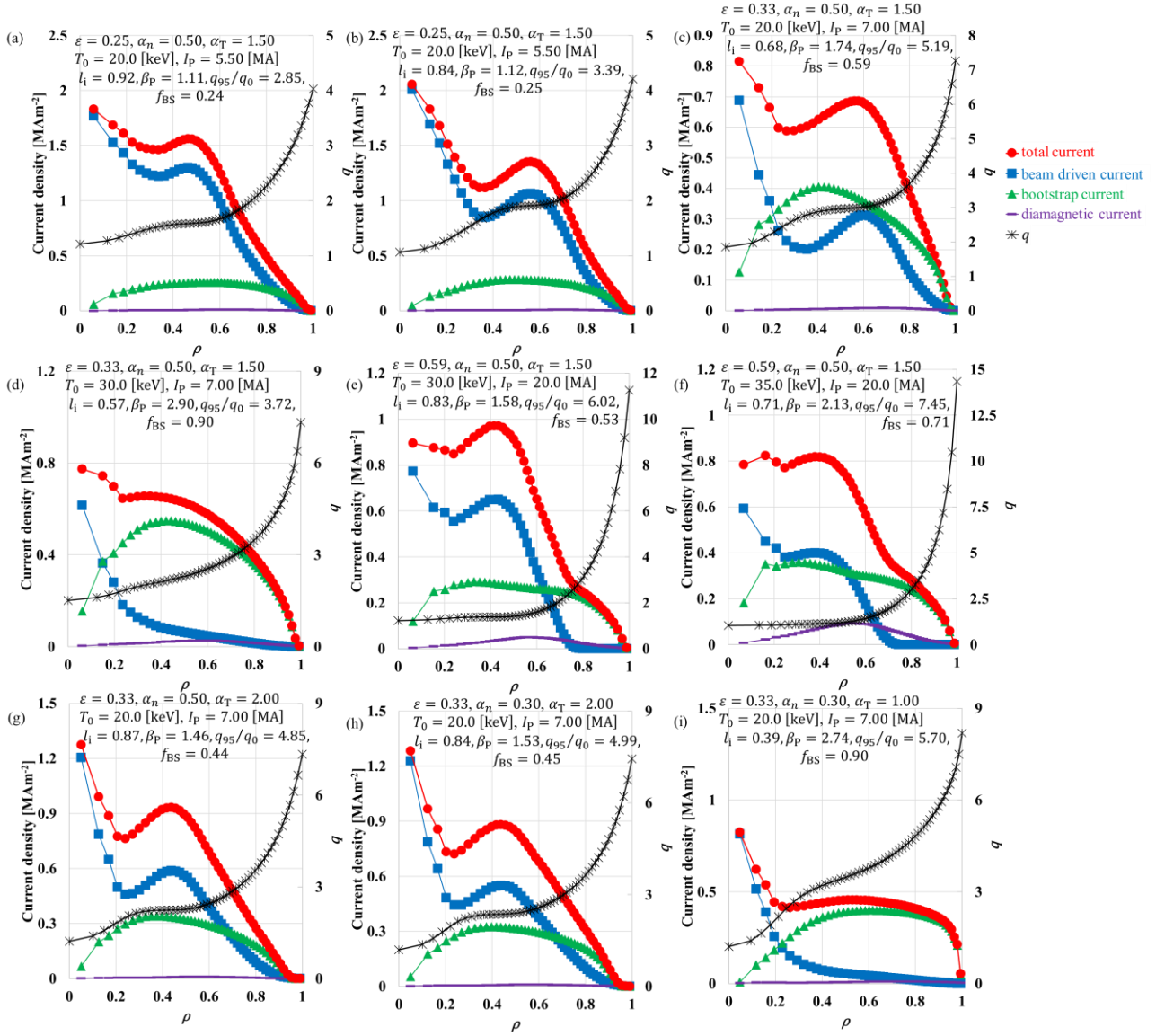


Fig. 14 The typical current density and q profiles of each type in the dataset for test #3. Panels (a)-(i) correspond to the types (I)-(IX) in Table 7, respectively.

positive shear profiles were included, as so in the fitting database. This similarity seems to be a cause of better accuracy of our scaling formulas in test #3 than in test #2.

In test #1, our formulas have a positive dependence on ε in contrast to nearly flat f_{BS} of the dataset. In test #2, the difference of the profile of the safety factor and the externally driven currents mainly cause of the relatively large errors of our formulas. In test #3, the condition of the dataset is relatively more similar to that of the fitting database, compared to that of test #2, the accuracy of our scaling formulas is improved in test #3. As shown in Table 5, in each test, our scaling formulas have similar RMSE. $f_{BS}^{\text{scaling}}(l_i, q, \varepsilon)$ seems to be applicable to tokamak plasmas with a wide range of parameters.

4. Summary and Conclusion

We constructed new scaling formulas for the bootstrap current fraction f_{BS} for tokamaks with full non-

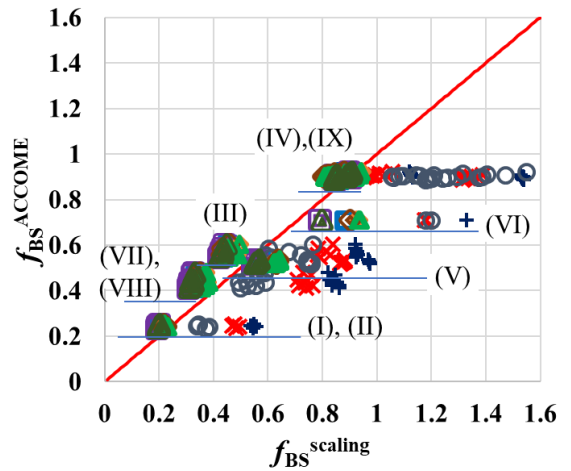


Fig. 15 The comparison between f_{BS}^{ACCOMME} and f_{BS}^{scaling} in test #3. The symbols are the same as those in Fig. 9.

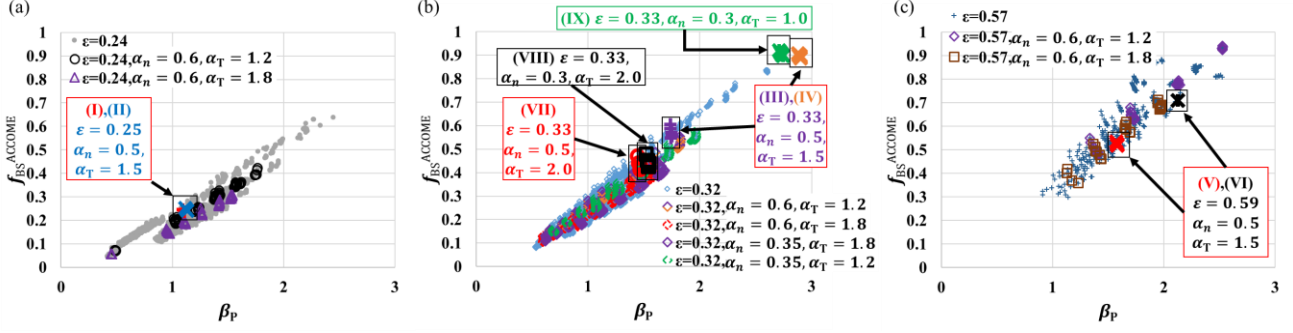


Fig. 16 The dependence of $f_{BS}^{ACCOMME}$ on β_p of the fitting database, (a) for $\varepsilon = 0.24$, with the case of (I) and (II) ($\varepsilon = 0.25$) for test #3, (b) for $\varepsilon = 0.32$, with the case of (III), (IV), (VII), (VIII) and (IX) ($\varepsilon = 0.33$) for test #3, (c) for $\varepsilon = 0.57$, with the case of (V) and (VI) ($\varepsilon = 0.59$) for test #3.

inductive operation with positive shear safety factor profiles, which are suited for 0-D system code analysis. The fitting database for scaling formulas was built by the ACCOME code [21] where two tangential units of neutral beam were employed for current drive and the plasma current density profile consistent with magnetohydrodynamics (MHD) equilibrium was obtained. The fitting database contained 12,150 self-consistent equilibria with relatively small plasma major radius of 2.44 m and safety factor q profiles satisfying $q(\rho) \geq 1.0$ and $q_{95} \geq 3.0$ in $0 \leq \rho < 1$, where ρ is the normalized minor radius and q_{95} is the q at the 95% poloidal flux surface.

From the fitting database, we conducted multiple regression analysis to derive the formulas. The formulas contained the inverse aspect ratio ε , the poloidal beta, and the profile shape indices for density and temperature profiles as well as parameters related to the q profile, the internal inductance l_i and/or the ratio of q_{95} to $q(0)$, q_{95}/q_0 , as input parameters. We evaluated the accuracy of the derived formulas by using the Root Mean Squared Error (RMSE). We built six formulas, by changing input parameters related to the q profile (l_i only, q_{95}/q_0 only, or both of l_i and q_{95}/q_0) and changing the multiple regression analysis methods (constant regression coefficients or those of linear functions of ε). The RMSE is the lowest (0.025) for the scaling using both of l_i and q_{95}/q_0 and with regression coefficients of linear functions of ε , $f_{BS}^{scaling(l_i, q, \varepsilon)}$, though difference in RMSE is not significant compared to other two formulas with regression coefficients of linear functions of ε and using l_i only or q only as parameters related to the q profile, $f_{BS}^{scaling(l_i, \varepsilon)}$ and $f_{BS}^{scaling(q, \varepsilon)}$.

We tested the derived formulas to three kinds of dataset different from the fitting database used for deriving the formulas. For comparison, the K. Gi models [18] and the ITER Physics Design Guidelines (IPDG) model [14] were also tested.

The first one was based on the aspect ratio scan in the neutron source study [11]. The plasma major radius was

$1.79 \text{ m} \leq R_p \leq 3.14 \text{ m}$. In this dataset, the RMSE of $f_{BS}^{scaling(l_i, q, \varepsilon)}$ was 0.069 though the dependence on ε was different. This different dependence on ε seems to be caused by the fact that parameters of the cases in this dataset were not well covered by the fitting database. The K. Gi models had the lowest RMSE (0.030 and 0.057).

The second one was the dataset used in [18], where the plasma major radius was 5.00 m. This dataset has the case of reversed shear. In this dataset, our scaling formulas underestimated f_{BS} in most cases and the RMSE of $f_{BS}^{scaling(l_i, q, \varepsilon)}$ was 0.179. The IPDG model had the lowest RMSE (0.047). The third one was the dataset built based on one used in [18] and in the second test. This contains only positive shear cases. The RMSE of the scaling $f_{BS}^{scaling(l_i, q, \varepsilon)}$ in this dataset was 0.076 and it was smaller than that of K. Gi models and the IPDG model. The reasons of better accuracy of our formulas in the third dataset than in the second dataset seem to be difference in the beam driven (externally driven) current profile as well as difference in the q profile. In the second and third tests, it is shown that the best derived formula is applicable for larger devices than the compact neutron source. These tests also covered a spherical tokamak (the plasma aspect ratio $A \leq 2$), a conventional tokamak ($A = 3 - 4$), and an advanced tokamak ($A = 3 - 4$, with relatively higher beta value).

Finally, it is concluded that the derived formula, $f_{BS}^{scaling(l_i, q, \varepsilon)}$ seems to be applicable to tokamak plasmas with a wide range of parameters.

Acknowledgements

This study was performed with the support of the Collaboration Research Programme of Joint Special Design Team for Fusion DEMO in Japan and of the Tokamak Plasma Collaboration Research Programme in National institutes for Quantum and Radiological Science and Technology.

Table A.1 The comparison result of ACCOME code analysis and the previous study [11] of main parameters

Parameter		Value	
		PEC [11]	ACCOMME
Total NB power of tangential injection [MW]	$P_{\text{NB}}^{\text{tan}}$	62	109.68
Current drive efficiency of tangential NB [$\text{Am}^{-2}\text{W}^{-1}$]	$\eta_{\text{NB}}^{\text{tan}}$	0.17×10^{20}	0.17×10^{20}
Gain for beam-thermal fusion of tangential NB	$Q_{\text{f}}^{\text{tan}}$	0.25	0.23
Quasi-perpendicular NB power [MW]	$P_{\text{NB}}^{\text{perp}}$	104	56.32
Current drive efficiency of quasi-perpendicular NB [$\text{Am}^{-2}\text{W}^{-1}$]	$\eta_{\text{NB}}^{\text{perp}}$	0.0	0.0017×10^{20}
Gain for beam-thermal fusion of quasi-perpendicular NB	$Q_{\text{f}}^{\text{perp}}$	0.50	0.50
Bootstrap current fraction	f_{BS}	0.62	0.45
Beam-thermal fusion power [MW]	$P_{\text{f}}^{\text{b-th}}$	67.5	53.0
Thermal-thermal fusion power [MW]	$P_{\text{f}}^{\text{th-th}}$	112.4	117.2
Total fusion power [MW]	$P_{\text{f}}^{\text{total}}$	180	170

Appendix A.

We compare fusion performance of tokamak neutron source evaluated by PEC [11] with that evaluated by ACCOME. As an example, we select the economically optimal case shown in Table 1 in [11], which is equivalent to the case of $A = 2.26$ of Table 4.

Main parameters of PEC code in the previous study [11] and of the ACCOME code analysis are compared in Table A.1. In both analyses, the tangential NB with beam energy of 800 keV and the quasi-perpendicular NB with beam energy of 200 keV were employed, with the fixed total NB power (166 MW). The lower beam energy of the quasi-perpendicular NB leads to higher gain for beam-thermal fusion than the tangential NB. The tangential NB power was determined to achieve the full non-inductive operation while the rest power was allocated to the quasi-perpendicular NB. In the previous study, f_{BS} was determined by the C. P. C. Wong model [12] given by Eqs. (17) to (19). The value of f_{BS} of ACCOME analysis includes the diamagnetic current. The f_{BS} obtained by the ACCOME analysis was lower than the value used in the previous study [11]. The decrease of f_{BS} results in higher $P_{\text{NB}}^{\text{tan}}$ and lower $P_{\text{NB}}^{\text{perp}}$ in the ACCOME analysis. As a result, the decrease of $P_{\text{NB}}^{\text{perp}}$ results in lower $P_{\text{f}}^{\text{b-th}}$ and lower $P_{\text{f}}^{\text{total}}$. This means a slightly larger (about 10%) thermal-thermal fusion power is needed to achieve the design value of total fusion power, 180 MW, which would result in a larger device size and a higher cost than those evaluated in [11].

References

- [1] [K. Yamazaki, et al., "Impact of plasma, magnet and wall performances on tokamak and helical reactor economics," Fusion Eng. Des. 81 \(2006\) 1145.](#)
- [2] [M. Kovari, et al., "'PROCESS': A systems code for fusion power plants—Part 1: Physics," Fusion. Eng. Des. 89 \(2014\) 3054–3069.](#)
- [3] H. Fujieda, et al., "Tokamak plasma power balance calculation code (TPC Code) outline and operation manual," JAERI-M (1992) 92–178 (in Japanese).
- [4] [J. Johner, "HELIOS-A zero dimensional tool for next step and reactor studies," Fusion Sci. Technol. 59 \(2011\) 308.](#)
- [5] [T. Hartmann, "Development of a Modular Systems Code to Analyse the Implications of Physics Assumptions on the Design of a Demonstration Fusion Power Plant," Technische Univ. Muenchen \(Germany\). Fakultät fuer Elektrotechnik und Informationstechnik \(2013\).](#)
- [6] [V. Menon, et al., "Physics Design and Analysis Code SPECTRE for Tokamak based Fusion Reactors," IAEA-FEC/FIP/P7-19 \(2014\).](#)
- [7] [C. Reux, et al., "DEMO reactor design using the new modular system code SYCOMORE," Nucl. Fusion 55 \(2015\) 073011.](#)
- [8] [Z. Dragojlovic, et al., "An advanced computational algorithm for systems analysis of tokamak power plants," Fusion Eng. Des 85 \(2010\) 243-265.](#)
- [9] [B. G. Hong, et al., "Development of a tokamak reactor system code and its application for concept development of a demo reactor," Fusion. Eng. Des. 83 \(2008\) 1615–1618.](#)
- [10] J. Wesson, Tokamaks, 4th ed. (2011), New York: Oxford University Press.
- [11] [T. Fujita, et al., "Optimization study of normal conductor tokamak for commercial neutron source," Nucl. Fusion 57 \(2017\) 056019.](#)
- [12] [C. P. C. Wong, et al., "Toroidal reactor designs as a function of aspect ratio and elongation," Nucl. Fusion 42 \(2002\) 547-556.](#)
- [13] W. M. Nevins, "Summary report: ITER specialists' meeting on heating and current drive,," ITER-TN-

PH-8-4, 13-17, June (1988).

- [14] [N. A. Uckan et al., "ITER Physics Design Guidelines: 1989," ITER Documentation Series, No. 10 \(1990\).](#)
- [15] [M C R Andrade and G O Ludwig, "Scaling of bootstrap current on equilibrium and plasma profile parameters in tokamak plasmas," Plasma Phys. Control. Fusion 50 \(2008\) 065001.](#)
- [16] [H. R. Wilson, "BOOTSTRAP CURRENT SCALING IN TOKAMAKS," Nucl. Fusion 32, \(1992\) 257.](#)
- [17] G. T. Hoang et al., "Bootstrap fraction in TFTR, Tore Supra and TEXTOR," Proc. 24th EPS Conference in Berchtesgarden Vol. 21A Part III (1997) 965.
- [18] [K. Gi, et al., "Bootstrap current fraction scaling for a tokamak reactor design study," Fusion Eng. Des. 89 \(2014\) 2709-2715.](#)
- [19] [O. Sauter, et al., "Neoclassical conductivity and bootstrap current formulas for general axisymmetric equilibria and arbitrary collisionality regime," Physics of Plasmas 6 \(1999\) 2834.](#)
- [20] [H. Lux, et al., "Uncertainties in power plant design point evaluations," Fusion Eng. Des. 123 \(2017\) 63-66.](#)
- [21] [K. Tani, et al., "Numerical analysis of 2D MHD equilibrium with non-inductive plasma current in tokamaks," J. Comp. Phys. 98 \(1992\) 332-341.](#)
- [22] [Y. Sakamoto, et al., "Characteristics of internal transport barriers in JT-60U reversed shear plasmas," Nucl. Fusion 41 \(2001\) 865.](#)
- [23] [Y. Sakamoto, et al., "Controllability of large bootstrap current fraction plasmas in JT-60U," Nucl. Fusion 47 \(2007\) 1506-1511.](#)
- [24] [T. Ozeki, et al., "EFFECTS OF A HOLLOW CURRENT PROFILE ON THE IDEAL MHD STABILITY," Nucl. Fusion 33 \(1993\) 1025.](#)
- [25] [Y. Sakamoto, "DEVELOPMENT OF PHYSICS AND ENGINEERING DESIGNS FOR JAPAN'S DEMO CONCEPT," IAEA-CN-258/FIP/3-2 \(2018\).](#)
- [26] [S. TOKUDA, et al., "Neoclassical MHD Equilibria with Ohmic Current," J. Phys. Soc. Jpn. 58 \(1989\) 871.](#)